ADVANCED MATERIALS INTERFACES

www.advmatinterfaces.de

Nanometer Resolved Real Time Visualization of Acidification and Material Breakdown in Confinement

*Claudia Merola, Hsiu-Wei Cheng, Dominik Dworschak, Ching-Shun Ku, Ching-Yu Chiang, Frank Uwe Renner, and Markus Valtiner**

Localized surface reactions in confinement are inherently difficult to visualize in real-time. Herein multiple-beam-interferometry (MBI) is extended as a real-time monitoring tool for corrosion of nanometer confined bulk metallic surfaces. The capabilities of MBI are demonstrated, and the initial crevice corrosion mechanism on confined nickel and a $Ni_{75}Cr_{16}Fe_9$ model material is compared. The initiation of crevice corrosion is visualized in real time during linear sweep polarization in a 1×10^{-3} M NaCl solution. Pre- and post-experiment analysis is performed to complementarily characterize the degraded area with atomic force microscopy (AFM), optical microscopy, nano-Laue diffraction (nano-LD), scanning electron microscopy (SEM)/ electron backscatter diffraction (EBSD), and X-ray photoelectron spectroscopy (XPS). Overall, $Ni_{75}Cr_{16}Fe_9$ displays a better corrosion resistance; however, MBI imaging reveals 200 nm deep severe localized corrosion of the alloy in the crevice opening. Chromium rich passive films formed on the alloy contribute to accelerated corrosion of the confined alloy by a strongly acidifying dissolution of the passive film in the crevice opening. Nano-LD further reveals preferential crystallographic defect and corrosion migration planes during corrosion. MBI provides nanometer accurate characterization of topologies and degradation in confined spaces. The technique enables the understanding of the initial crevice corrosion mechanism and testing modeling approaches and machine-learning algorithms.

1. Introduction

Due to their high corrosion resistance in various aggressive environments, nickel and nickel alloys are widely used in different sectors of industry, including e.g., petrochemistry or power generation. However, in the presence of chloride, these materials display considerable susceptibility to corrosive degradation.[1,2] Despite the enormous body of literature and work that was performed over recent decades on corrosion of Ni-based alloys, crevice, and pitting attacks, which take place in confined and localized spots respectively, are very difficult to detect and to study in real time.[3–9] Further, it is currently not yet possible to quantitatively predict localized corrosion due to a limited mechanistic understanding of initial steps. In order to prevent or limit localized corrosive attacks, nickel can be alloyed with different elements to improve resistance[10] against localized corrosion.

Chromium as an alloying element reduces the corrosion rate by passivating the surface of the metal and increases the pitting potential. The breakdown of the passivity of the material is then related to the local dissolution of the passive chromium oxide film from the surface.[11] In this case, literature suggests that the chromium oxide film generally hinders the diffusion of oxygen from solution to the active metal surface and increases the anodic dissolution potential.[12–19]

The initiation and growth of pitting corrosion should be observed in aerated halide solutions only in those metals whose critical potential is lower than the reversible oxygen electrode (E_{SHE} = 0.8 V). For example, metals like Cr and Ti that have their critical potential over 1 V are not expected to suffer from pitting corrosion.[20]

However, there is a different situation in the case of crevice corrosion, where the media are stagnant and the concentration

Dr. C. Merola, Dr. H.-W. Cheng, D. Dworschak, Prof. M. Valtiner
Institute of Applied Physics
Vienna University of Technology
Vienna 1040, Austria
E-mail: valtiner@iap.tuwien.ac.at

The ORCID identification number(s) for the author(s) of this article can be found under https://doi.org/10.1002/admi.201802069.

© 2019 The Authors. Published by WILEY-VCH Verlag GmbH & Co. KGaA, Weinheim. This is an open access article under the terms of the Creative Commons Attribution-NonCommercial License, which permits use, distribution and reproduction in any medium, provided the original work is properly cited and is not used for commercial purposes.

DOI: 10.1002/admi.201802069

Dr. C. Merola
Max-Planck-Institut für Eisenforschung GmbH
Department for Surface Chemistry and Interface Engineering
Duesseldorf 40237, Germany

Dr. C.-S. Ku, Dr. C.-Y. Chiang
Materials Science Group
National Synchrotron Radiation Research Center
300 Taiwan

Prof. F. U. Renner
Institute for Materials Research (IMO)
Hasselt University
Diepenbeek BE3590, Belgium

Prof. F. U. Renner
IMEC vzw. Division IMOMEC
Diepenbeek BE3590, Belgium

of aggressive species can accumulate. With proceeding corrosion reactions, a simultaneous decrease in pH, increase in chloride concentration, and depletion of oxygen occurs. This results in a breakdown of the passivity and enhanced corrosion in a crevice, as well as generally lower critical corrosion (i.e., passivity breakdown) potentials for most alloys. For instance, for stainless steels, according to Fujimoto et al.,[21] a threshold concentration of around 10% chromium is required, so that a stable layer of Cr_2O_3 can form to protect an alloy from corrosion. Ebrahimi et al.[22] and Marcus and Grimal[23] showed through X-ray photoelectron spectroscopy (XPS) measurements that the resistance of the passive film is controlled by Cr_2O_3 and that once the transpassive potential region is reached, the resistance of the film decreases with a parallel increment of $Cr(OH)_3$ content in the film. Once the passive film breaks down, and dissolution becomes stable, the role of the chromium is to effectively repassivate the crevice. Nagarajan and Rajendran[24] also observed that superaustenitic stainless steels show an increase of the roughness inside the crevice using optical and atomic force microscopy (AFM) imaging.[25] For materials that exhibit an active-to-passive transition, the IR drop that develops inside of a tight crevice can further explain the location of corrosion initiation.[26–30] According to this model pioneered by Pickering,[31] inside a crevice a potential drop (IR drop) and hence a specific local potential distribution occurs due to increased resistance and/or increased passive currents due to changes of the solution chemistry[32] inside of a crevice. This IR drop can essentially shift the local potential from the passive into the active region of a material.

While literature on crevice corrosion is vast and well-advanced,[26,33–35] development of methods to view crevice corrosion in real time and at initial stages are notoriously difficult to develop. We recently[36] developed an interferometric technique for studying the initial crevice corrosion of vapor deposited or sputtered metal thin films (with thicknesses in the range of 20–60 nm) under the influence of confined geometries by using a modified transmission mode surface forces apparatus (tSFA). This setup provides valuable information to explore the initiation of pitting and crevice corrosion[36] of thin films. However, thin films often have a distinctly different microstructure compared to bulk alloys. The limitation of the tSFA is thus a drawback that greatly restricts the investigation of commercially available alloys, and effects of microstructure. In this work, we resolved this shortfall, and designed a reflection mode equipped surface forces apparatus (rSFA) for operation with nontransparent bulk metal samples. The idea of the rSFA was first tested by Connor and Horn[37] to study the interface between mica and a mercury droplet. Unlike the tSFA, the observed fringes of equal chromatic order (FECO) produce an intensity decrease of the interference pattern in rSFA due to the optical arrangement and light absorption within the interferometer cavity. Yet still, the information available about the confinement geometry can be calculated to the same precision as tSFA. The rSFA can however be used to study any sufficiently reflecting bulk material, including most commercial alloys.

Here, we discuss the newly designed rSFA, which is specifically tailored for generating crevices with well-defined geometries. We test its performance using pure nickel and a $Ni_{75}Cr_{16}Fe_9$ model alloy and we complement this work by extensive pre- and postanalysis of the samples used, utilizing optical microscopy, topography analysis using an atomic force microscope. We also characterize the samples using electron backscattering diffraction (EBSD) and nano-Laue diffraction (nano-LD),[38,39] to characterize local crystal orientation,[40] grain boundaries,[41] and deformation around pits forming[42] at the corroding crevices.

2. Results and Discussion

2.1. Crevice Corrosion of Nickel and a $Ni_{75}Cr_{16}Fe_9$ Alloy

To test the performance of the newly designed rSFA (for details see the Experimental Section), we studied two different material types that are prone to crevice corrosion. Specifically, we use pure nickel and a $Ni_{75}Cr_{16}Fe_9$ model alloy. Addition of chromium results in the formation of a very stable Cr-rich passive layer, and a lower susceptibility to corrosion is expected for the alloy. Standard anodic linear sweep voltammetry (LSV) with a scan rate of 1 mV s^{-1} (Figure S2, Supporting Information) confirms the expected behavior with a shift of the critical potential of the $Ni_{75}Cr_{16}Fe_9$ to more anodic potentials by about 250 mV compared to pure Ni, indicating the increased corrosion resistance of the alloy.

2.1.1. Crevice Formation and Overview of the Recorded Crevice Corrosion Process in an rSFA

In **Figure 1**, we first demonstrate the crevice formation for both materials in the newly designed rSFA. Specifically, Figure 1a,b shows how rSFA may be used to generate a confined area with precise control for nickel and the $Ni_{75}Cr_{16}Fe_9$, respectively. Generally, the local elliptical geometry of the crevice can be well-controlled in terms of the confined area, A_C, which is adjusted to a major axis diameter of about 300 µm for both examples.

The opening angle depends on the local curvature of the crevice former and indicates the expected larger opening angle along the minor axis of the ellipse. In general, the opening angle is slightly variable within 0.5° due to gluing the crevice former onto a glass disc. Experimentally, opening angles along the minor axis can be varied by varying the glass disc radius, which is an aspect that we did not study in detail in this work. The measured contact geometry of the confinement geometry is indicated as a relief map in the figure as well. Irrespective of the lack in very precise control of the opening angle, the major advantage of interference microscopy is that it allows us to directly and precisely measure any established confinement geometry. Opening angles and contact reliefs can be measured based on a nanometer precision, interference-based, distance measurement between the apposing surfaces at any point of the sample contact during the experiment. Even grain boundaries and differences in grain heights can be well-resolved. This is clearly visible in the enlarged image of the established Ni contact shown in Figure S3 in the Supporting Information).

The small inset in Figure 1a,b shows the wavelength resolved interference pattern (FECO) recorded across the contact as indicated. The constant wavelength of each standing wave in the

© 2019 The Authors. Published by WILEY-VCH Verlag GmbH & Co. KGaA, Weinheim

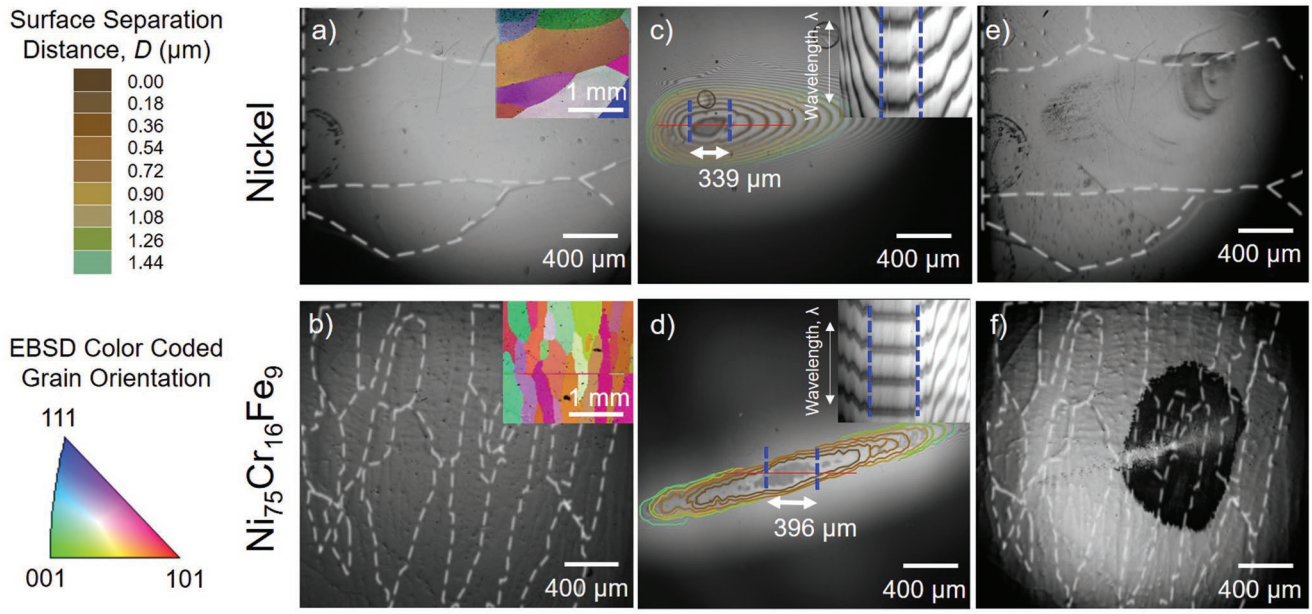

Figure 1. Establishing and characterization of confined zones. Newton's rings (NR) of mirror polished surfaces of a) nickel and b) $Ni_{75}Cr_{16}Fe_9$ confined by a cylindrical mica surface. The Newton's rings were color coded to indicate a contact geometry based on an NR analysis. Confinement geometries are further illustrated as inset figures of (a,b) showing typical FECO recorded for the samples. c,d) Grain boundaries on these optical images are indicated with white dashed lines based on EBSD characterizations, shown as inset figures for c) nickel and d) $Ni_{75}Cr_{16}Fe_9$. e,f) Samples after corrosion, respectively. Samples were washed with milli-Q water and dried in a flow of N_2 prior to image acquisition.

center of the contact, marked by the dotted blue lines, indicates that the confined zone is flat to within the roughness of the metal surface. Using the shift of these standing waves with respect to the dry contact allows us to directly calculate the thickness of the fluid film in confinement, which is estimated to be between 2.5 and 3.5 nm at open circuit potential (OCP).

Prior to starting a corrosion experiment, all samples were routinely characterized by using EBSD and optical microscopy. Figure 1c,d shows an overview of the optical images together with the corresponding EBSD pattern and grain orientations recorded for the same area where the confined area is established. The Ni sample appears to have considerably larger grains compared to the alloy. We can now correlate grain sizes and orientation to the confined area corroded in experiments.

Figure 1e,f shows ex situ optical images of Ni and $Ni_{75}Cr_{16}Fe_9$ samples, respectively, after corrosion occurred at the confined areas. Interestingly, the corrosion mechanism of both materials proceeds completely different. Generally, Ni samples show pitting inside the confined area A_C and in an area A_O around the confined area within the crevice opening. In contrast, the $Ni_{75}Cr_{16}Fe_9$ shows considerably less pitting inside of the nanometer confined area A_C, but a very pronounced corrosion in the area A_O of the crevice opening. The black region in the optical microscopy is due to severe corrosion and increased surface roughness in this region, which results in significant scattering of the incoming light.

Detailed Real-Time View of the Corrosion Process Using rSFA Interference Pattern: Apart from establishing very well characterized confined areas and postexperimental inspection of the corroded area shown in Figure 1, the rSFA allows us to analyze the corrosion process in real time. Therefore a time-resolved sequence of interferometric images is recorded during linear sweep polarization. Images can be recorded with real time frame rates up to 100 Hz with our equipment. Here, we typically record with frame rates of 2 Hz, as the recorded processes are comparably slow. Representative images of the entire corrosion process are shown in Figure S3 in the Supporting Information for nickel and in **Figure 2** for the alloy.

The onset of corrosion on nickel and the $Ni_{75}Cr_{16}Fe_9$ appears at around 0.35 and 0.6 V versus Ag|AgCl, respectively. At this critical potential, the initiation of crevice corrosion in the Newton's rings (NRs) pattern was very obvious for the $Ni_{75}Cr_{16}Fe_9$, but it was less pronounced in the Ni sample (see Supporting Information for details), where we find increased pit formation at the confined zone, and less dense pitting outside. Interestingly, the $Ni_{75}Cr_{16}Fe_9$ displays a much more severe local corrosion mechanism. Figure 2a–c shows time-resolved NR patterns recorded during the LSV scan for the alloy, and Figure 2d shows the final corrosion damage recorded after the experiment.

Specifically, the NR in Figure 2a–c shows a very pronounced change of the standing waves, which is indicative of progressing local corrosive damage. In addition, a significant decrease of the light intensity can be visualized at the corroding site, due to roughness increase and resulting scattering of light. The NR change and intensity changes in the confined zone can be viewed as a fingerprint of the changing confinement geometry and ongoing corrosive degradation, respectively.

Detailed analysis of the corrosion behavior of the $Ni_{75}Cr_{16}Fe_9$ shown in Figure 2a–c reveals several noteworthy characteristics, which are initiation from a single site in the confined

© 2019 The Authors. Published by WILEY-VCH Verlag GmbH & Co. KGaA, Weinheim

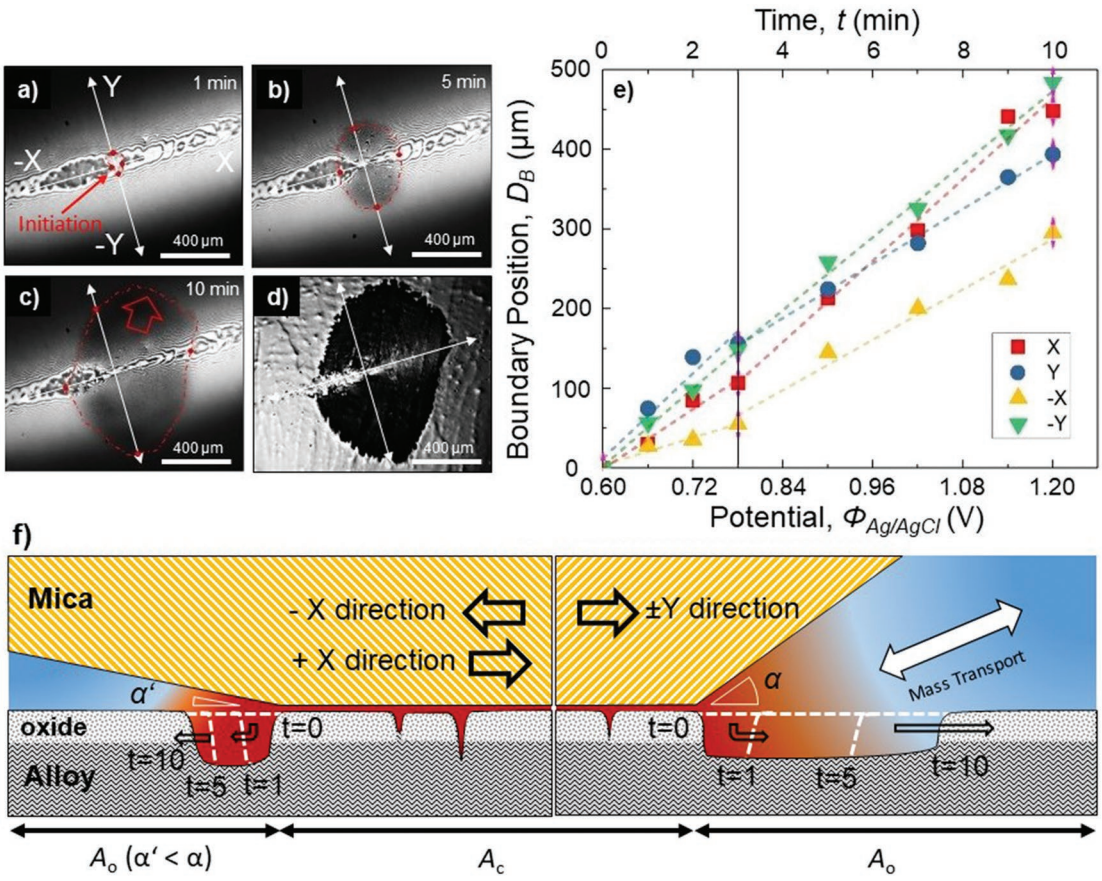

Figure 2. Real-time corrosion analysis. a–d) Screen-shots of the video of the corrosion progress at different times (+1, +5, +10 min and after corrosion). e) Lateral crevice corrosion progression along the major elliptical axis (*X*) and (*Y*) for $Ni_{75}Cr_{16}Fe_9$ plotted against the time/applied potential. The vertical line indicates that all directions progress with approximately similar rates. f) Schematic of corrosion mechanism around the area of confinement for both samples. The local pH increase is indicated (red shaded area).

area, directional and grain dependency along with a weakly pronounced potential dependency.

First, in this example and in general, the corrosion of the confined $Ni_{75}Cr_{16}Fe_9$ initiated at a single specific location (marked by an arrow in the displayed example) within the confined area A_c for all probed samples. From this location, corrosion progressively propagated out in all spatial directions. This behavior is consistent with the diffusive propagation of an aggressive crevice environment, starting from a particular initiation site. This is consistent with the strongly acidifying breakdown of the protective Cr_2O_3 into soluble chromate, which releases 10 protons per formula unit as follows

$$Cr_2O_{3(s)} + 5H_2O_{(l)} \rightarrow 2CrO^{2-}_{4(aq)} + 6e^- + 10H^+_{(aq)} \quad (1)$$

At the final stage as shown in Figure 2c,d after mica has been removed, a very pronounced dark corroded region on $Ni_{75}Cr_{16}Fe_9$ was observed. This dark region coincides with the lower intensity that propagated in the real time NR images and is marked with red dashed lines in the interferometric images in Figure 2 a–c.

In contrast, on pure Ni (see again Figure 1e), pitted areas were observed inside, and in the close vicinity of, the confined zone, and general roughening and to a lesser degree pitting was observed over the entire surface. Interestingly, and as can be seen in the figure as well, specifically grains with vicinal orientations close to (111) show an increased pitting also outside of the confined zone. Considering that the anodic dissolution of nickel only generates 2 protons per unit formula, the less significant corrosive attack of nickel in the confined zone can be explained by the less acidic local environment as well. In addition, the observed roughening is in good agreement with weaker protective properties of the passive film on nickel, which dissolves at the applied potentials according to the nickel Pourbaix diagram.

We additionally performed XPS analysis of the surface chemistry of the corroded region and outside of the confined regions, for both materials. Data are shown in Figures S4/S5 in the Supporting Information. For the $Ni_{75}Cr_{16}Fe_9$ alloy, the data indicate that the oxide composition inside and outside of the crevice shows a very clear trend of $Ni(OH)_2$ depletion and Cr_2O_3 as well as Fe_2O_3 enrichment. This further confirms the expectation, that a passive Cr_2O_3 layer is enriched at the surface, and that its breakdown results in a strong acidification of the crevice environment according to Equation (1). XPS of the nickel surface revealed the expected formation of a $NiO/Ni(OH)_2$ layer,

© 2019 The Authors. Published by WILEY-VCH Verlag GmbH & Co. KGaA, Weinheim

Table 1. Lateral propagation rate for the $Ni_{75}Cr_{16}Fe_9$ along the major and minor axes of the confined zones.

Average speed [μm min^{-1}]	*X*-direction	*Y*-direction	−*X*-direction	−*Y*-direction
0–3 min	37.6 ± 4.2	53.4 ± 9.6	17.4 ± 2.6	48.7 ± 2.1
3–10 min	51.1 ± 3.6	34.3 ± 1.1	31.6 ± 2.9	45.9 ± 2.3

which may slowly dissolve in a mildly acidic environment of a crevice on nickel.

Second, the shape of the corroded region at the final stage displays a weakly pronounced anisotropy, which cannot be explained by an isotropic diffusive spreading of aggressive electrolyte. This may rather be due to both the crevice opening geometry and the grain orientation. As indicated in Figure 2a–d, this anisotropic progression can be decoupled into individual progression rates along the four principal directions of the elliptical contact area. Figure 2e shows the tracking of the boundary position of the corroded region along these directions as a function of the applied potential/time. From the slope of this plot, lateral propagation rates can be calculated (see **Table 1**).

Interestingly, corrosion initially propagates slower along the ±*X*-axis compared to the ±*Y*-direction. In particular, along the −*X*-direction (confined region), the propagation is two times slower compared to the *Y*-directions, and also significantly slower compared to +*X*. As sketched in the schematic in Figure 2f, this is due to the limited diffusion rate of the aggressive electrolyte along the fully confined −*X*-direction, caused by the different crevice opening angle, and due to confinement and, hence, the possible saturation of the only 2–3 nm thick confined electrolyte. At a potential above 0.78 V, the −*X*-direction proceeds faster as well. This may be due to spreading of the aggressive environment at larger crevice opening distances, where diffusion into the −*X*-direction is not limited by confinement any longer.

In the later stages it appears that corrosion, due to a slightly slower progression along the +*Y*-direction, shows a directional tendency (see Figure 2c, red arrow), that follows the grain orientation. The preferential propagation direction is in line with the overall orientation of the grains in this region, which are oriented in (*X*,*Y*) to (−*X*,−*Y*) direction. Interestingly, this suggests that grain orientation dependency only plays a minor role during the initial spreading of crevice corrosion, and only evolves at a later stage as a minor influence.

In comparison, it is interesting to summarize that the rSFA data indicate that 1) Ni corrosion proceeds as pronounced localized pitting and roughening with statistically more pitting inside the confined zone and in general on specific grains. For pure nickel, which shows an active-to-passive transition, the localization of the more severe localized attack within the crevice is fully consistent with an IR-drop[31] driven initiation of the corrosion. Specifically, and as can be observed in Figure 1e, pitting is maximal in regions where the separation distance is around 0.5–0.9 μm (compare to color code and confinement location in Figure 1e), which may be the area where the local potential drops into the active region of nickel corrosion. In contrast, 2) the $Ni_{75}Cr_{16}Fe_9$ shows an apparently more severe areal attack in the opening of the confined zone. In this case, the attack proceeds from an initial critical breakdown at one specific site. These results are consistent with severe confinement acidification and accelerated breakdown of material in the immediate surroundings of the initial breakdown site due to the spreading of aggressive crevice solution. For the alloy, it appears that we can follow the diffusion of the aggressive environment in real time. This is similar to the behavior found for Ni thin films in our earlier work.[36] The alloy also exhibits no active-to-passive transition at the neutral bulk pH values used in our work. A clear active-to-passive transition only occurs at pH values below pH = 1 (data not shown). This suggests that for crevice corrosion to initiate a sufficiently aggressive crevice solution must first develop to initiate breakdown of the passivity. In our experimental setting, this appears to occur at a region where the electrolyte film is in the tens of nanometer range (i.e., at the rim of the fully confined zone where only a 2–3 nm thin electrolyte exists). For such thin electrolytes, even the passive current may initiate passivity breakdown, which can autocatalyze and hence accelerate the breakdown according to Equation (1). This suggests that the critical crevice solution model is better suited to explain the location where the breakdown occurs. However, the outward motion of the corrosive attack seems at odds with such an interpretation as it may not be possible to maintain the acidic conditions while progressing toward the opening of the crevice. The observed outward motion during propagation is consistent with an IR-drop driven propagation after initiation. Given the applied linear ramp potential, it is also not clear how the local potentials evolve. To further understand mechanistic aspects and in order to compare to theoretical models, experiments at constant potential are needed. However, here we focus on the experimental development of the technique and focus our discussion on demonstrating the in situ capabilities.

2.1.2. Postexperiment Analysis of the Corroded Areas

While interference images along with FECO patterns in the rSFA provide a real time view into a confined zone, they are also restricted to the Abbe limit of optical microscopy at about 200 nm local resolution. Hence, nanoscaled structure changes during the corrosion process remain unresolved in situ. For instance, nanoscale roughening, which is a surface modification well below the Abbe limit, is only visible as an average broadening of the FECO pattern. In this section, we hence complement the rSFA data with AFM imaging to provide high spatial resolution of both materials after corrosion, and we recorded nanoscale Laue diffraction of corroded regions after corrosion to provide further nanoscopic understanding of the processes visualized in rSFA.

High-Resolution AFM Imaging: **Figure 3** shows AFM images recorded at different areas of the corroded region for both materials used. Figure 3a,d shows an optical image of the corroded regions for the Ni and the Ni alloy, respectively. The labeled areas indicate where the AFM topographies displayed in panels (b,c) and (e–g) were recorded, respectively. The recorded AFM images reveal a number of interesting details and highlight the different mechanism observed for the Ni and the Ni alloy, as follows (also see schematic interpretation in Figure 3h).

© 2019 The Authors. Published by WILEY-VCH Verlag GmbH & Co. KGaA, Weinheim

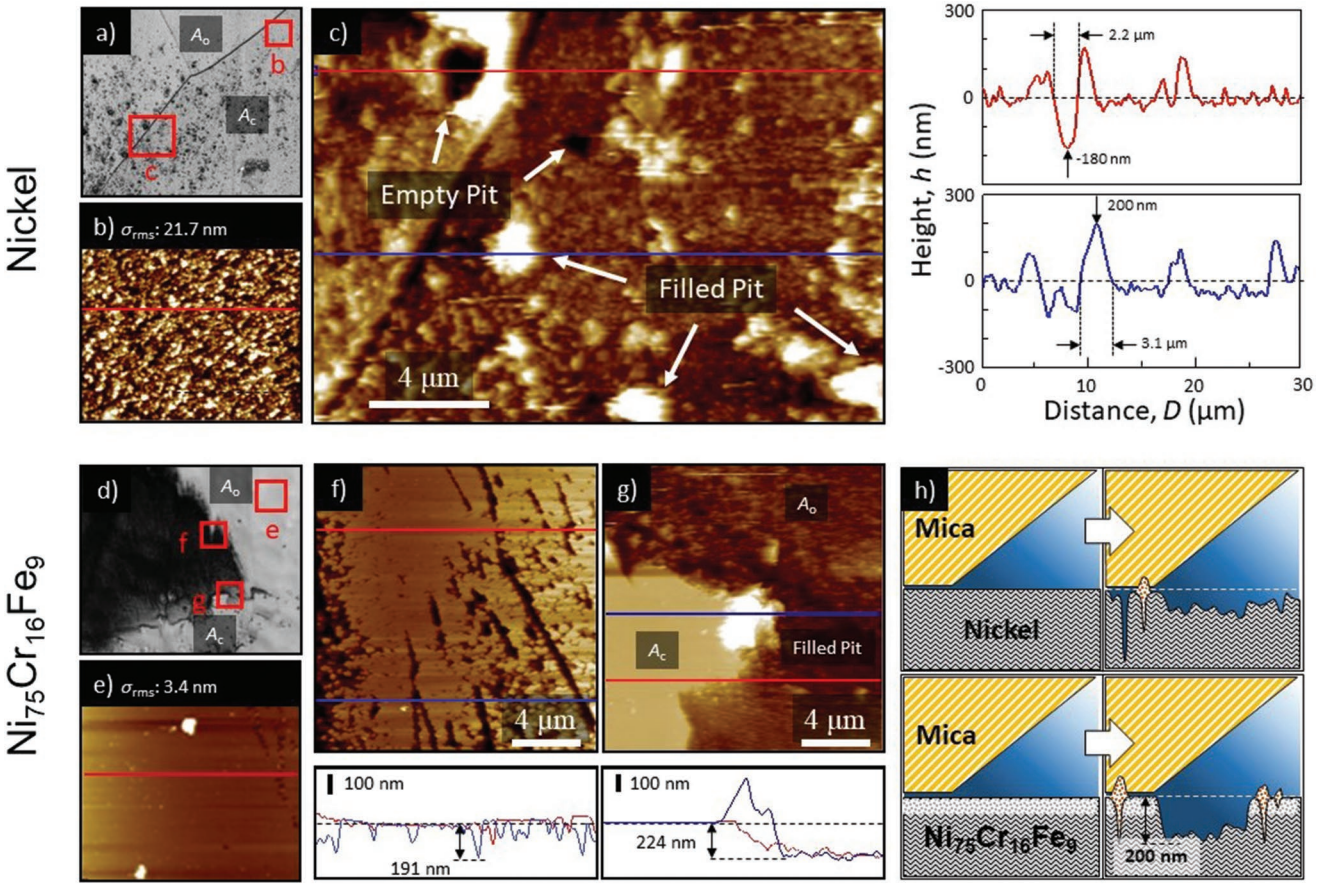

Figure 3. Postexperiment analysis of the corrosion area with AFM. a) Optical image of the confined area of the nickel. AFM images of the surface of the nickel after the corrosion experiment b) outside the confinement, and c) inside the crevice area. In (c), two lines indicate cross-sections shown on the right of the image. The red line indicates the cross-section over a pit, while the blue line is a cross-section of a pit presumably filled with precipitates. d) Optical image of the $Ni_{75}Cr_{16}Fe_9$ after corrosion. e) AFM topography inside the confinement that was not attacked by the corrosion. The surface is still as smooth as after polishing, in contrast, Ni undergoes significant roughening away from the contact region. f) On the edge of the black region, the two lines indicate the cross-sections and the graph is reported below. g) An AFM scan over a precipitate filled pit inside the confined region. h) Schematic representation of the corrosion process for Ni and $Ni_{75}Cr_{16}Fe_9$ around the crevice former.

First, the region outside of the confined area of the corroded Ni shown in Figure 3b indicates a severe roughening with a roughness of $\sigma_{rms} \approx 22$ nm, compared to the initial 2–3 nm before corrosion (not shown). This indicates a rather uniform dissolution process across the entire surface of pure nickel, in addition to the increased pitting probability in confinement. The same roughness level is also found within the confined area shown in Figure 3c, where denser pit formation is observed as well. The respective height profiles for Figure 3c indicate that corrosion pits are at least 180–200 nm deep. This depth should be viewed as the lower bound due to possible geometric restrictions by the AFM tip geometry. Interestingly, apart from roughening and pit formation, also large protrusions up to 180–200 nm appear around pits, or presumably on top of a pit. This may indicate corrosion products that are precipitating in the confined area during the corrosion process due to saturation of the electrolyte, ending up in pits filled with precipitated oxide/hydroxide.

Second, and in stark contrast, the AFM topography in Figure 3e indicates that $Ni_{75}Cr_{16}Fe_9$ shows no significant roughening, neither outside the corroding area of the crevice opening, nor in the fully confined zone. However, within the crevice opening, where the surfaces are only a few 100 nm apart, the corrosion is more severe compared to the pure nickel. Specifically, at the progression front, shown in Figure 3f, severe and dense pitting with pitting depths of about 200 nm occurs. As indicated in Figure 3g and the respective height profile pits coalesce into a rough and ≈200 nm deep corroded area that extends into all spatial directions initiating from the rim of the fully confined zone. Pit coalescence was previously observed for other nickel-based alloys in chloride containing solutions.[30]

The location of the roughening is consistent with the region that was observed to spread in the rSFA data. Interestingly, Figure 3d,g shows that the fully confined area A_C does not show any roughening, and only pitting with a much smaller density compared to the pure Ni. It is visible in Figure 3g as well, that we again find—presumably precipitate-filled—pits in this region with a very similar height compared to the Ni case. This is a generally interesting result and suggests that the confined zone, where the electrolyte is only 2–3 nm thick, is

© 2019 The Authors. Published by WILEY-VCH Verlag GmbH & Co. KGaA, Weinheim

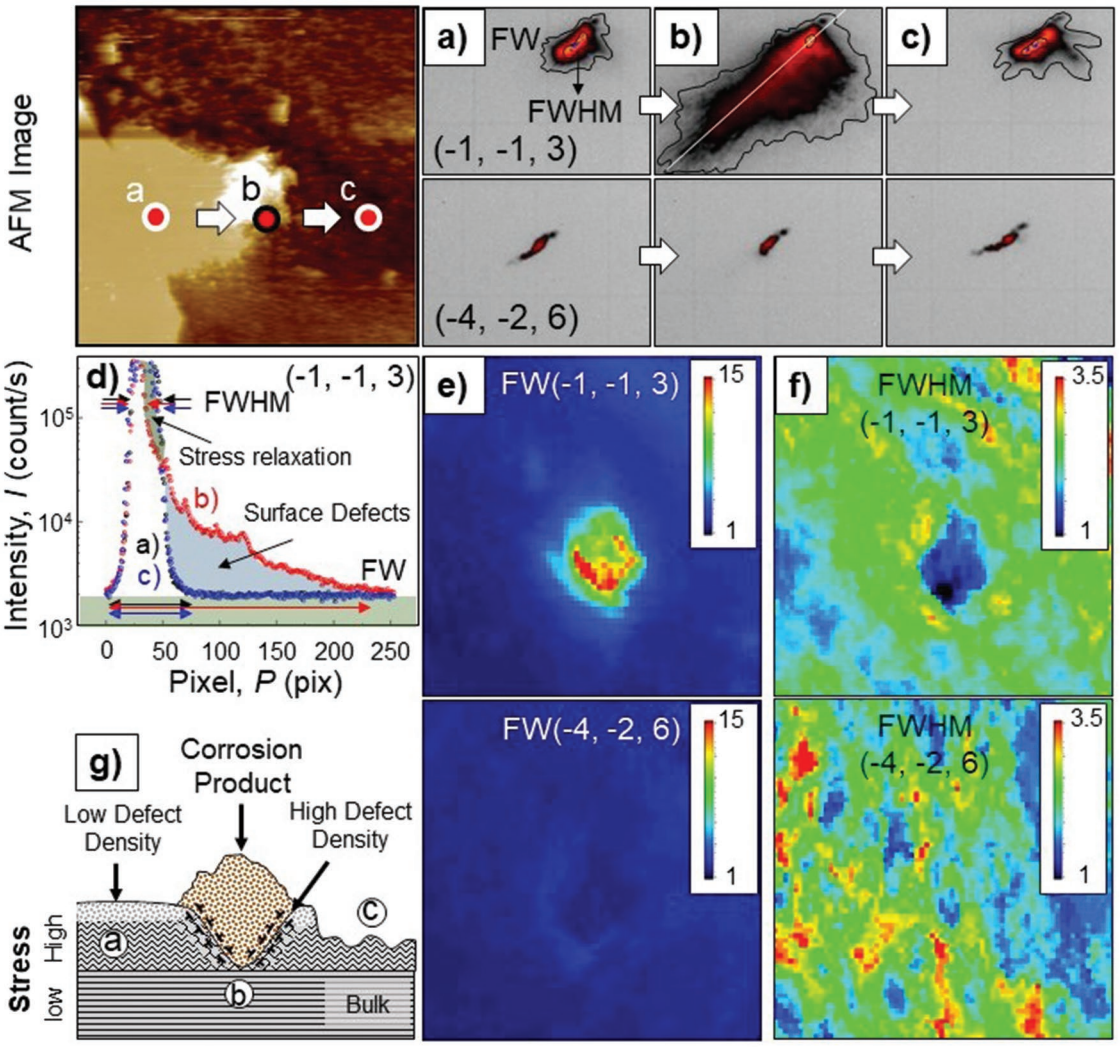

Figure 4. Nano-Laue X-ray diffraction analysis. Characteristic Laue reflections of two characteristic orientations (–1, –1, 3) and (–4, –2, 6) are plotted in (a–c). These patterns were acquired at locations indicated in the AFM image. Variation of the peak shapes are also shown in (d) as line profiles plotting pixel number against logarithmic intensity. Any change of the full width (FW) and full width at half maximum (FWHM) of the scattering peak relates to surface defects and size of crystalline domains, respectively. In (e,f), FW and FWHM of the Laue peaks are plotted as a function of the location, corresponding to the area shown in the AFM image. A schematic interpretation of results is illustrated in (g) (c.f. text for details).

better protected, presumably due to saturation of the solution. In addition, the severe reaction within the crevice opening again suggests that the chromium contributes to a significant acidification of the environment according to Equation (1). This, in turn, leads to a faster corrosion in this area, where exchange with the bulk electrolyte may still be limited, maintaining a sufficiently aggressive crevice solution. As discussed above, the propagation may also be driven by an IR-drop model.

Crystal Structure and Defects in Corroded Areas: Apart from the local geometric factors in a crevice environment, other contributing factors to corrosion are the crystal or grain structure and stress. To evaluate how defects contribute to local corrosion, we further studied corroded regions of rSFA samples with nano-Laue diffraction. This method is able to provide locally resolved stress and dislocation density maps for any crystallographic plane after corrosion occurred.

Figure 4 shows results of the nano-LD based analysis for the region where corrosion initiated for the $Ni_{75}Cr_{16}Fe_9$ alloy. The indexed scattering patterns (see Figure S6 in the Supporting Information) confirm that the alloy structure is a nickel-based face centered cubic (fcc) crystal structure with some nickel atoms replaced by chromium and iron.

A detailed analysis of nano-LD intensity and specifically of the shape and distribution of the pattern on the 2D detector further provides information on full width area (FW), corresponding to the surface defect density, and full width half maximum area (FWHM) corresponding to the size of ideally crystalline domains. Specifically, the increase of the FW, which characterizes the low intensity broadening of the diffraction peak, is due to surface defects. Furthermore, internal stress in grains leads to the distortion of the entire bulk crystal structure resulting in a broadening of the FWHM. Therefore, for FW and FWHM, an increased value indicates an increased surface

© 2019 The Authors. Published by WILEY-VCH Verlag GmbH & Co. KGaA, Weinheim

defect density and an increased bulk deformation, respectively. For more details on the method, the reader is referred to relevant literature.[43,44]

For the alloy, Figure 4a–c compares the Laue peak shapes for specific reflections (–1, –1, 3) and (–4, –2, 6) recorded at the points indicated in the AFM image, shown as reference. Among all the diffraction peaks collected by the detector, characteristic peaks (Figure 4a–c) are representative for all observed peaks (see Figure S7 in the Supporting Information for further collected Bragg reflections). These patterns indicate two interesting aspects.

First, these representative reflections show a very stark difference. Reflection (–4, –2, 6) shows hardly any low intensity broadening of the FW at different locations, while the FW of reflection (–1, –1, 3) is very sensitive to the location. Specifically, (–1, –1, 3) indicates a significant increase of the FW, i.e., a low intensity peak broadening, in the region of the central pit. A comparison of line scans (marked by the white indication line in (a–c)) of the recorded intensity profile further illustrates this effect in Figure 4d. Second, and in stark contrast to the FW, the FWHM decreases within the pit compared to outside of the pit for this facet.

Figure 4e,f shows a mapping of the FW and FWHM over the entire region shown in the AFM image, respectively. This provides a 2D overview of surface defect densities and bulk lattice distortions. The results further detail how the surface defect density (FW) is significantly increased inside the pit. It is interesting that this localized defect increase only appears for particular reflections, specifically (–1, –1, 3) and (–3, –1, 5) (see again Figure S7 in the Supporting Information). In contrast, e.g., for (–4, –2, 6) and many other reflections, the analysis indicates that the pit is "invisible" as compared in Figure S7 in the Supporting Information. This is a very interesting observation and general phenomenon that suggests that corrosion in the pit is fueled by surface defect migration and corrosion progression along particular crystallographic facets as indicated in the schematic in Figure 4 g.

Hence, we can conclude that corrosion proceeds along a particular facet of the alloy, which accumulates a higher surface defect density.

The nonintuitive finding that the FWHM appears significantly less broad in the pit region is also interesting (see Figure 4f). This suggests that a locally deeper probe volume, where corrosive damage is not yet detectable, contributes to the recorded signal. This may be due to the lower scattering cross-section of the corrosion products within the pit, suggesting corrosion products that are amorphous. This interpretation is supported by the fact that there are no additional peaks that relate to corrosion products deposited within the pit. As such, the corrosion products, that appear to be within the filled pits observed in the AFM scan, are very likely amorphous, which fits a fast reprecipitation reaction after supersaturation of the local environment in a pit.

3. Conclusions

rSFA is a unique real-time tool for making very well characterized confined areas on real samples for testing corrosion in confinement. It provides a detailed in situ view into a corroding crevice on reflective bulk metals. Together with a complementary set of extensive postcorrosion analyses, it is possible to generate a detailed understanding of the corrosion of any bulk material. The measured confinement geometry in an rSFA may serve as a very well defined experimental reference for testing modeling approaches.

For the studied model systems, namely, Ni and the $Ni_{75}Cr_{16}Fe_9$, we can summarize the following conclusions:

- The corrosion mechanism of pure Ni proceeds via severe roughening (from σ_{rms} = 2–3 nm to σ_{rms} = 20 nm) and pitting over the entire surface, with an increased pitting density of about 200 nm deep pits in the vicinity of and inside the nanometer confined zone, which is fully consistent with an IR-drop model. In contrast, $Ni_{75}Cr_{16}Fe_9$ shows no significant corrosion outside the confined area.
- $Ni_{75}Cr_{16}Fe_9$ exhibits two distinctly different areas in the confined region. In the fully confined area, no severe corrosion occurs and only pitting at much lower density compared to Ni is found. In contrast, within the crevice opening, severe corrosion via coalescence of very dense pits results in a severely rough area with about 200 nm deep material loss. It is peculiar, that pitting seems to consistently propagate 200 nm into the material, irrespective of the gap size. This may be due to a progressing local saturation of the crevice solution, or due to significant defect accumulation in the first 200 nm of the surface due to polishing. The latter seems unlikely based on the nano-Laue data.
- Severe crevice corrosion of the alloy may be attributed to the local autocatalytic acidification, which was visualized in real time with rSFA. Local acidification spreads with a lateral progression rate of 17–50 μm min^{-1}, due to fast and significant proton release during passive film breakdown which may maintain a sufficiently aggressive crevice solution. How the local potential evolves, and to which degree the IR drop drives the propagation remains unclear, and potentiostatic experiments will be essential in future work.
- Similar to transmission mode SFA, reflection mode experiments may provide a path into analyzing refractive indices of the crevice solution in situ. Such a capability may allow more detailed views into initiation conditions and modeling.
- Based on the material loss and in situ lateral progression rate of the corrosion recorded using the rSFA, we can estimate the local current of $Ni_{75}Cr_{16}Fe_9$ corrosion in the crevice opening to be at least >0.1 A cm^{-2}.
- Nano-LD results reveal that pit propagation proceeds along particular facets of the alloy, and corrosion products deposited in pits do not show any crystalline structure, indicating a fast precipitation due to saturation of the local environment.

4. Experimental Section

Chemicals and Materials: High purity sodium chloride was purchased from Sigma-Aldrich and a 1 $\times 10^{-3}$ M solution was prepared with Milli-Q (Millipore) water with a resistivity >18 MΩ cm and a total organic carbon (TOC) value <2 ppb. Optical grade V1 ruby-mica was obtained from S&J Trading Company as sheets of about 20 cm × 20 cm and 2 mm thickness. Surfaces were prepared using 5–10 cm^2 mica sheets with

© 2019 The Authors. Published by WILEY-VCH Verlag GmbH & Co. KGaA, Weinheim

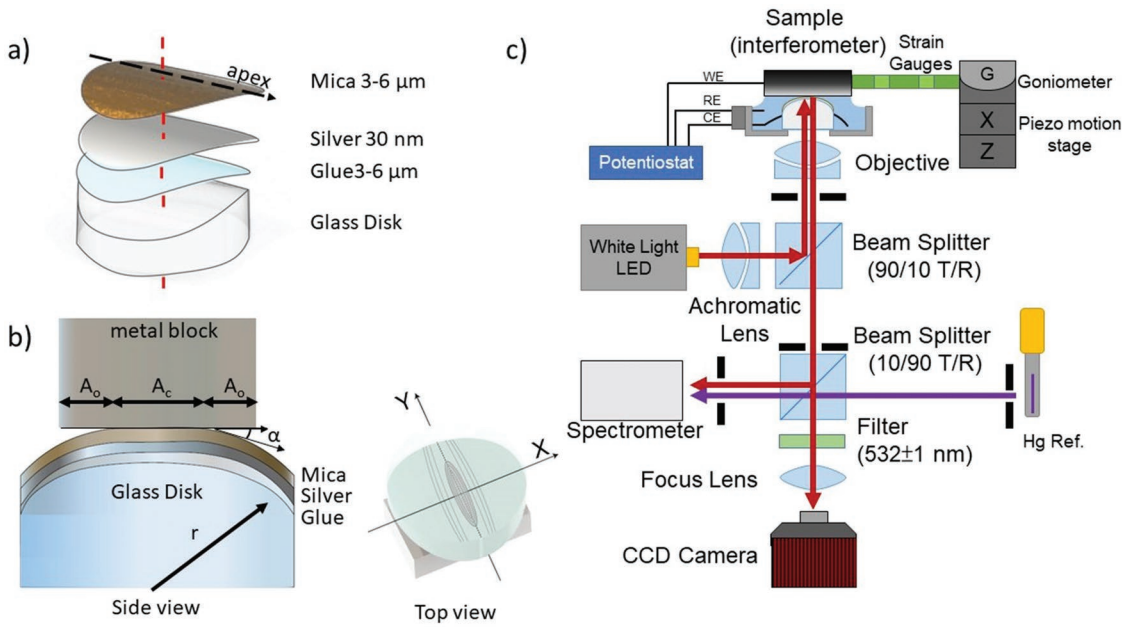

Figure 5. a) Detailed view of the compliant crevice former. b) Detailed schematic of the sample arrangement (c.f. text for details). A_c and A_o indicate the area of contact and the area outside of confinement where the apposing surfaces are separated by less than a few µm. Upon contact with the metal block, the glued mica layer can comply with the surface topology of the metal, forming a flat confined contact area with elliptic shape. c) Schematic view of a surface forces apparatus in reflection mode (rSFA). The white light path is represented by the red line, it is guided through a beam splitter where 10% of incident achromatic white light is reflected onto the interferometer. The objective simultaneously focuses onto and collects the light from the sample, at the second (10/90 T/R) beam splitter 10% is projected onto the CCD camera for Newton's rings observation. The other 90% is collected at the spectrometer, where the fringes of equal chromatic order (FECO) are observed. The sample acts as the working electrode, Pt wires are used as both counter and reference electrodes. A goniometer together with a set of *XY*-translation stages are used to fine tune the tilt angle and contact position of the sample.

thicknesses ranging from 2 to 5 µm, which were hand-cleaved from raw sheets and used for the experiments.[45] These highly flexible sheets of mica, back-coated with silver, were then glued to cylindrical silica disks of nominal radius of curvature $R = 7–15$ mm.

Preparation of Model Alloys: Alloys were prepared at the Max-Planck-Institut für Eisenforschung. The single elements had a high purity above 99.99% and they were cast in an oven. Cast ingots were used as is, cut into pieces with a total width of 5 mm. The metal blocks were then first ground with sand paper of different grain sizes (from P80 to P2500), then polished with diamond paste of 0.05 µm and finally polished with a colloidal silica suspension to a mirror finish. Afterward, samples were extensively cleaned and sonicated in pure water. XPS results (below) indicated no contamination above 2–3% of a monolayer coverage equivalent.

Surface Forces Apparatus: Crevice corrosion experiments were performed in a confined geometry generated in a newly designed rSFA. The setup and its optics were home built using components from Thorlabs, including a sCMOS camera (2.1 Megapixel), a laser line filter 532 ± 1 nm, two beam splitters (10/90 and 90/10), objective with a 4× magnitude, an Andor spectrograph coupled with an IXON 3 EMCCD camera, and a MWWHL4 LED as white light source (WL). **Figure 5** shows a sketch of the major components of this setup. Here, materials and methods used for crevice formation are briefly discussed; below, the optical setup and general considerations will be discussed in more detail.

Figure 5a shows the typical confining surface layout used as a crevice former. Specifically, a molecularly smooth, back-silvered muscovite mica surface was glued on a glass cylinder. Using the layered-silicate muscovite mica provided a molecularly smooth and transparent crevice former that can be produced with very small thickness by manual cleavage.[45] The silver coating at the back-side was semitransparent (40 nm silver thickness) and provided the mirror surface for generating an interferometer. As shown in Figure 5b, the apposing metal blocks (Ni, Alloy) with 5 mm height and 5 mm diameter were mounted on the top sample holder with their fine polished surface apposing the crevice former. With these two mirrors, a 2-layer interferometer was generated. Any changes in the separation distance between the Ag and the metal mirror, due to e.g., ingress of water, or shift of the metal mirror surface by corrosion (conversion into oxide or dissolution), can be tracked with time by analyzing standing waves in the optical cavity that is generated. Further details on white light interferometry can be found here by Israelachvili.[46]

Once corrosion occurs, clear changes in the wavelength of standing waves in the interferometer cavity (e.g., due to shift of the reflecting surfaces due to corrosive consumption of the metal) as well as changes of the light intensity of the Newton's rings can be detected with an optical microscope of 4× magnitude by projecting the image on a CCD camera and a spectrometer equipped with a sCMOS sensor (Andor, Zyla), respectively.

Atomic Force Microscopy: AFM images were recorded in tapping mode with an Asylum Research Cypher AFM using photo thermal excitation to oscillate the cantilever. The measurements were performed with gold-coated cantilevers (Arrow-UHF-AuD, Nano World) with a length of 35 µm, resonance frequency of 0.7–2 MHz. The images were postprocessed using plane leveling implemented in the Asylum software package.

Nano-Laue Diffraction: Synchrotron experiments were performed at Taiwan Photon Source (TPS) Beamline 21A at the National Synchrotron Radiation Research Center (NSRRC), Taiwan. This beamline was dedicated to white light Laue diffraction for structural analysis (e.g., phase identification, grain orientations, residual strain, stress, and dislocation mappings). A schematic of the beamline capabilities is provided in Figure S1 in the Supporting Information. The estimated spatial resolution for such measurements can regularly reach 80 × 80 × 50 nm at this beamline. Therefore, the beamline utilizes a preshaped

© 2019 The Authors. Published by WILEY-VCH Verlag GmbH & Co. KGaA, Weinheim

Kirkpatrick–Baez mirror pair to focus the polychromatic X-ray beam with energies ranging from 5 000 to 30 000 eV.

The sample was navigated inside the chamber with online real-time scanning electron microscopy (SEM) with a spatial resolution of 4 nm, allowing the correlation of locations to SFA measurements. The station mount allowed the sample position to be adjusted in three dimensions, and was situated on an active vibration isolation table. All measurements were performed in vacuum. The specimen was mounted on a specially designed sample stage with 45° pretilted angle relative to the incident X-ray beam.

Diffraction patterns were collected using a high sensitivity hybrid pixel array detector (PAD, PILATUS3-X-6M), located at the focus point above the sample (angle resolution better than 0.018°). Diffraction patterns were analyzed using the XMAS software package[47] to identify the crystal phases, while the mapped images of total intensity, crystal orientation, and peak width were calculated using a LabVIEW-based code.

Electrochemistry: All measurements were performed in 1×10^{-3} M NaCl solution. Every Pt pseudo reference used in rSFA experiments was referenced against a standard 3N Ag|AgCl electrode, showing a difference of about +200 mV with typical variations of 50–80 mV depending on the Pt wire used. All data are referenced to the Ag|AgCl potential for comparison.

To ensure that the recorded electrochemical signal in the rSFA was related to the polished surface, all samples were first sealed with epoxy glue, and then polished to the desired surface finish. In the rSFA corrosion experiments were conducted using a three-electrode system with platinum wires as both reference and counter electrodes, and Ni or the alloy block as the working electrode. Experiments were reproduced multiple times with similar outcomes. All potential ramp rates were 1 mV s^{-1}, and were initiated at E_i: −0.1 V versus open circuit potential, and scanned to an upper limit of E_f = 1.5 V versus E_{ref}, if not stated otherwise below. An emStat 3+ potentiostat (Palmsense) was used for all electrochemical measurements.

Scanning Electron Microscopy and Electron Backscatter Detection: SEM and EBSD analysis was performed at the USTEM facility at Vienna University of Technology, working on an FEI Quanta 250 FEG with a beam energy of 10 keV.

X-Ray Photoelectron Spectroscopy: All XPS measurements were performed with a Quantum 2000 (Physical Electronics). Spectra were measured using the implemented high power mode, where photoelectrons were generated by a continuous scanning of a 100×100 μm^2 sized X-ray spot (100 W) over an area of 100×1000 μm^2 in order to minimize X-ray damage to the sample. Pass energy and scan steps were 22.5 and 0.2 eV for high resolution element scans, and 104 and 0.4 eV for survey spectra acquisition. To obtain a good signal-to-noise ratio, 15 and 30 sweeps for the C 1s and metal signals, were used respectively. All binding energies were referenced against the adventitious C 1s signal at 284.8 eV.

Operating Principle and Construction of a Surface Forces Apparatus for Reflection Mode Application: Since its invention several decade ago, the SFA principle has been used in different geometries, and for generating confined spaces. Several groups pioneered the utilization of SFA to study degradation, dissolution,[36] and more general chemical reactivity in confined spaces.[48] Figure 5 shows the major components of the newly designed rSFA adapted for operation with bulk metal samples. The crevice former in Figure 5a consists of a molecularly smooth back-silvered mica (for details refer to *Surface Forces Apparatus* in the Experimental Section) glued to a glass cylinder with a nominal radius R = 1 cm. Mica as a crevice former mimics a typical insulator/metal interface, while mica may exhibit higher surface charges compared to other ceramic materials. The crevice former is compliant due to the deformable glue. If the cylindrical shaped crevice former is pressed against a flat mirror polished metal surface (see Figure 5b), undulations of the glued mica surface and compliance result in flat elliptical contact zones, while small variations of the metal grain heights (e.g., due to polishing effects) can also result in confining the highest grains that are in contact with the apex of the cylinder.

Typical major and minor axis diameters of the confined area were in the range of 300 and 100 μm, respectively, resulting in confined areas of A_C = 0.03 mm^2. The typical electrolyte thickness T_{fl} in the confined area can be directly measured using white light interferometry and was within the range of 0.5–3 nm, which also depended on the electrochemically applied charging conditions within the crevice,[36] i.e., applied potentials vary the electric double layer thickness at a given normal load. In general, cylinder on flat experiments cannot apply pressures that are high enough to fully dehydrate hydrophobic interfaces.

The elliptic shape of an established crevice also results in different crevice opening angles for the major and minor elliptical axis. Depending on the radius of the disc used, the contact radius of the confining crevice former, can be varied from 5 mm < R < 40 mm, allowing control of the opening angle of the minor axis within a limited range between 5° and 15°. As can be seen from Figure 5b, we also indicate an area around the confined zone, where the crevice opening is typically increasing the distance between the apposing surfaces to some hundreds of nanometers, characterized by an area of A_O.

Figure 5c shows the optical setup, the major motion degrees of freedom, and the electrochemical cell. First, the sample, a Pt-CE and a Pt-RE were connected to a potentiostat, as described in the Experimental Section. Second, a contact was established and aligned using a sample stage with coarse and piezo-based fine motion in xyz. A goniometer allowed us to align the apex of the crevice forming cylinder parallel with respect to the flat metal surface. The metal sample was additionally mounted to springs equipped with strain gauges for measuring lateral and normal forces to 1) assist with the alignment, and 2) to set a normal force and hence a pressure at the contact zone. Typical applied pressures in this work were around 2–3 bar. Third, interference microscopy and white light interferometry were realized using a home built reverse microscope setup, with an LED white light source. Collimated WL is guided into a 4× microscope objective using a beamsplitter with a 90 to 10 splitting, for transmission out of the path, and reflection into the confined zone and interference cavity, respectively. The light reflected from the interferometer cavity using a beam splitter (ratio 10/90) was then guided through an additional beam splitter to simultaneously record both 1) a microscopic interference image on a CCD camera, and 2) fringes of equal chromatic order in a spectrometer. The optical path was filtered through a green 532 nm laser line filter to specifically visualize the standing waves at 532 nm, i.e., to visualize so called Newton's rings generated by the interferometer cavity. Both, NR and FECO provided a measure for the dimensions of the confined area, with NR only providing a thickness resolution of about 2–5 nm,[46] while FECO were accurate to within a few tens of picometer. Finally, a mercury reference lamp was guided into the spectrometer in parallel, in order to verify and calibrate the spectrometer.

Supporting Information

Supporting Information is available from the Wiley Online Library or from the author.

Acknowledgements

The authors acknowledge the support of the European Research Council in the framework of the ERC Starting Grant CSI.interface, grant number 663677 (development of reflection mode SFA). The authors also acknowledge the scientific staff at beamline 21A (TPS, NSRRC) for technical support. They also thank H. Springer for supplying model alloy samples.

Conflict of Interest

The authors declare no conflict of interest.

© 2019 The Authors. Published by WILEY-VCH Verlag GmbH & Co. KGaA, Weinheim

Keywords

crevice corrosion, Laue diffraction, nickel, passive films, surface forces apparatus

Received: December 23, 2018
Revised: February 11, 2019
Published online: April 25, 2019

[1] N. J. Laycock, J. Stewart, R. C. Newman, *Corros. Sci.* **1997**, *39*, 1791.
[2] G. S. Frankel, L. Stockert, F. Hunkeler, H. Boehni, *Corrosion* **1987**, *43*, 429.
[3] D. V. V. Moll, R. C. Salvarezza, H. A. Videla, A. J. Arvia, *J. Electrochem. Soc.* **1985**, *132*, 754.
[4] C. G. P. Tomashov, N. D. Tomashov, G. P. Chernova, O. N. Marcova, *Corrosion* **1964**, *20*, 166t.
[5] A. A. Seys, M. J. Brabers, A. A. Van Haute, *Corrosion* **1974**, *30*, 47.
[6] H.-H. Strehblow, *Mater. Corros.* **1976**, *27*, 792.
[7] J. M. Kolotyrkin, *Corrosion* **1963**, *19*, 261t.
[8] G. S. Frankel, *J. Electrochem. Soc.* **1998**, *145*, 2186.
[9] Z. Szklarska-Smialowska, *Corrosion* **1971**, *27*, 223.
[10] K. H. Sarmiento, N. S. Zadorozne, R. B. Rebak, *Acta Metall. Sin. (Engl. Lett.)* **2017**, *30*, 296.
[11] M. Urquidi, D. Macdonald, *Electrochem. Soc. Ext. Abstr.* **1985**, *85*, 29.
[12] M. Sakashita, N. Sato, *Corros. Sci.* **1977**, *17*, 473.
[13] B. C. Syrett, D. D. Macdonald, H. Shih, *Corrosion* **1980**, *36*, 130.
[14] C. M. Wylie, R. M. Shelton, G. J. P. Fleming, A. J. Davenport, *Dent. Mater.* **2007**, *23*, 714.
[15] J. R. Hayes, J. J. Gray, A. W. Szmodis, C. A. Orme, *Corrosion* **2006**, *62*, 491.
[16] M. Schütze, R. B. Rebak, R. Bender, *Corrosion Resistance of Nickel and Nickel Alloys Against Acids and Lyes*, Wiley-VCH, Weinheim **2014**.
[17] L. Guojin, G. Zangari, *Electrochim. Acta* **2002**, *47*, 2969.
[18] N. A. S. Sampaio, J. W. J. Silva, H. A. Acciari, R. Z. Nakazato, E. Codaro, H. Felipe, *Mater. Sci. Appl.* **2010**, *01*, 369.
[19] N. S. Zadorozne, C. M. Giordano, M. A. Rodríguez, R. M. Carranza, R. B. Rebak, *Electrochim. Acta* **2012**, *76*, 94.
[20] J. Horvath, H. H. Uhlig, *J. Electrochem. Soc.* **1968**, *115*, 791.
[21] S. Fujimoto, R. C. Newman, G. S. Smith, S. P. Kaye, H. Kheyrandish, J. S. Colligon, *Corros. Sci.* **1993**, *35*, 51.
[22] N. Ebrahimi, P. Jakupi, J. Noël, D. Shoesmith, *Corrosion* **2015**, *71*, 1441.
[23] P. Marcus, J. M. Grimal, *Corros. Sci.* **1992**, *33*, 805.
[24] S. Nagarajan, N. Rajendran, *Corros. Sci.* **2009**, *51*, 217.
[25] H. Ogawa, H. Omata, I. Itoh, H. Okada, *Corrosion* **1978**, *34*, 52.
[26] R. G. Kelly, J. S. Lee, *Encyclopedia of Interfacial Chemistry, Localized Corrosion: Crevice Corrosion* (Ed: K. Wandelt), Elsevier, Amsterdam **2018**.
[27] M. T. Woldemedhin, J. Srinivasan, R. G. Kelly, *J. Solid State Electrochem.* **2015**, *19*, 3449.
[28] J. Srinivasan, R. G. Kelly, *Corrosion* **2017**, *73*, 613.
[29] R. Lillard, M. Jurinski, J. Scully, *Corrosion* **1994**, *50*, 251.
[30] R. Lillard, J. Scully, *J. Electrochem. Soc.* **1994**, *141*, 3006.
[31] H. Pickering, *J. Electrochem. Soc.* **2003**, *150*, K1.
[32] B. Nash, R. Kelly, *Corros. Sci.* **1993**, *35*, 817.
[33] L. Lazzari, *Pitting and Crevice Corrosion*, European Federation of Corrosion (EFC) Series, Woodhead Publishing **2017**.
[34] A. Zaki, *Types of Corrosion: Materials and Environments*, Butterworth-Heinemann, Oxford **2006**.
[35] J. Kruger, S. Begum, *Reference Module in Materials Science and Materials Engineering, Corrosion of Metals: Overview*, Elsevier, Amsterdam **2016**.
[36] C. Merola, H. W. Cheng, K. Schwenzfeier, K. Kristiansen, Y. J. Chen, H. A. Dobbs, J. N. Israelachvili, M. Valtiner, *PNAS* **2017**, *114*, 9541.
[37] J. N. Connor, R. G. Horn, *Rev. Sci. Instrum.* **2003**, *74*, 4601.
[38] J. Ulaganathan, A. G. Carcea, R. C. Newman, R. I. Barabash, N. S. McIntyre, *Surf. Interface Anal.* **2017**, *49*, 1442.
[39] L. N. Brewer, D. P. Field, C. C. Merriman, *Electron Backscatter Diffraction in Material Science, Mapping and Assessing Plastic Deformation Using EBSD in Material Science*, Springer, New York **2009**, pp. 251–262.
[40] E. Y. Ma, Y. T. Cui, K. Ueda, S. Tang, K. Chen, N. Tamura, P. M. Wu, J. Fujioka, Y. Tokura, Z. X. Shen, *Science* **2015**, *350*, 538.
[41] K. Chen, M. Kunz, N. Tamura, H. R. Wenk, *Geology* **2015**, *43*, 219.
[42] A. Mehta, X. Y. Gong, V. Imbeni, A. R. Pelton, R. O. Ritchie, *Adv. Mater.* **2007**, *19*, 1183.
[43] G. Zhou, W. Zhu, H. Shen, Y. Li, A. Zhang, N. Tamura, K. Chen, *Sci. Rep.* **2016**, *6*, 28144.
[44] A. S. Budiman, W. D. Nix, N. Tamura, B. C. Valek, K. Gadre, J. Maiz, R. Spolenak, J. R. Patel, *Appl. Phys. Lett.* **2006**, *88*, 233515.
[45] J. N. Israelachvili, N. A. Alcantar, N. Maeda, T. E. Mates, M. Ruths, *Langmuir* **2004**, *20*, 3616.
[46] J. N. Israelachvili, *J. Colloid Interface Sci.* **1973**, *44*, 259.
[47] N. Tamura, A. A. MacDowell, R. Spolenak, B. C. Valek, J. C. Bravman, W. L. Brown, R. S. Celestre, H. A. Padmore, B. W. Batterman, J. R. Patel, *J. Synchrotron Radiat.* **2003**, *10*, 137.
[48] J. Dziadkowiec, S. Jayadi, J. E. Bratvold, O. Nilsen, A. Royne, *Langmuir* **2018**, *34*, 7248.

© 2019 The Authors. Published by WILEY-VCH Verlag GmbH & Co. KGaA, Weinheim